

<https://doi.org/10.1038/s43246-024-00471-x>

# Continuous iron spreading on carbon-shell composite nanotubes for electromagnetic wave absorption

Check for updates

Yuanyuan Zhang<sup>1</sup>, Yining Li<sup>1</sup>, Can Zhang<sup>1</sup>, Zhenjie Guan<sup>1</sup>✉, Liang Zhen<sup>1,2,3</sup> & Jiantang Jiang<sup>1,2</sup>✉

Iron-based nanotubes are promising candidates for high performance electromagnetic wave absorbing fillers due to their high aspect ratio, light weight, high axial permeability and high saturation magnetization. Furthermore, the introduction of carbon can improve dielectric loss and block the agglomeration of iron nanotubes. Here, Fe@C composite nanotubes were prepared by introducing carbon onto the surface of precursor  $\alpha$ -FeOOH' fibers followed by hydrogen-thermal annealing. We find that Fe@C composite nanotubes retain the one-dimensional nanostructure of the precursor throughout the annealing. The well-developed lattice and nanostructure of Fe@C nanotubes endow high saturation magnetization, high anisotropy, suppressed eddy current effect and cross-particle exchange coupling as well, and thus contribute to an enhanced permeability. Coatings with Fe@C as fillers achieve a reflection loss of up to  $-69.34$  dB at 3.37 GHz at the matching thickness of 3.97 mm. The Fe@C composite nanotubes developed here are a promising candidate for high performance electromagnetic wave absorbing fillers.

To develop electromagnetic wave absorbing (EMA) materials that can present high efficiency in broad band is a long-lasting but ever-newing mission. High and well-matched electromagnetic properties are cornerstones for achieving excellent EMA performance. To bring beneficial effects together to excavate the potential of component materials is thus basically crucial. High saturated magnetization, high anisotropy, and suppressed eddy current effect, together with the cross-particle exchange coupling, are believed factors that benefit permeability. On the other hand, the properly tailored conductivity and the overlap of nanotubes/nanofibers can also contribute to strong dielectric/conducting loss. The most effective way to achieve these beneficial effects is to prepare composite structures of low dimension and nanoscale<sup>1</sup>. Specifically, the introduction and integration of ferromagnetic components on the nanometer scale is critical for balancing the ferromagnetic properties, the conductivity, the cross-particle exchange coupling, and the dielectric loss. Many researches have been carried out in the past few decades to explore the feasibility of obtaining high EMA efficiency from fabricating nanocomposite structures while many obstacles still survive.

The preparation and electromagnetic properties of one-dimensional (1D) ferromagnetic absorbers with high shape anisotropy are increasingly favored by researchers in the field of EMA

materials. To compare with equiaxed particles, 1D ferromagnetic particles contribute much more to dielectric loss, eddy current loss, and ferromagnetic loss as well, in the EMA materials. Liu et al.<sup>2</sup> anchored NC/Co nanosheets vertically on the surface of hollow HCF fibers, where Co nanoparticles were uniformly dispersed on the outer surface of carbon nanosheets. Che and coworkers successfully prepared TiO<sub>2</sub>@Co/C@Co/Ni multilayered microtubes in which Co/Ni nanoparticles were uniformly distributed on the outer surface of the fibers<sup>3</sup>. It was noted that, well-matched dielectric and ferromagnetic work together and therefrom enhance the propagation and attenuation of the incident microwaves. Zhang et al.<sup>4</sup> prepared Fe/SiC hybrid fibers via an electrospinning process and noted that the introduction of Fe particles promoted the growth of amorphous nanowires on the surface of SiC fibers and then contributed evidently to the improved permittivity and permeability. Luo et al.<sup>5</sup> prepared FeCo@CFs hybrids using an electrodeposition process and found that the EMA properties of FeCo@CFs hybrids can be tailored by adjusting the morphology of Fe/Co coating. Jiang et al.<sup>6</sup> decorated Co particles on the surface of Al<sub>18</sub>B<sub>4</sub>O<sub>33</sub> whiskers and therefrom achieved high EMA efficiency. These researches focused on the external decorating of dielectric components by introducing ferromagnetic metal particles

<sup>1</sup>School of Materials Science and Engineering, Harbin Institute of Technology, Harbin 150001, China. <sup>2</sup>National Key Laboratory of Precision Hot Processing of Metals, Harbin Institute of Technology, Harbin 150001, China. <sup>3</sup>Sauvage Laboratory for Smart Materials, School of Materials Science and Engineering, Harbin Institute of Technology (Shenzhen), Shenzhen 518055, China. ✉e-mail: [guanzy@hit.edu.cn](mailto:guanzy@hit.edu.cn); [jitcy@hit.edu.cn](mailto:jitcy@hit.edu.cn)

on substrate fibers of the micrometer scale. These efforts encountered some limitations in excavating the potential of ferromagnetic/dielectric components owing to the nature of the composite structure constructed. For instance, the presence of the high conductive metal coating on the outer surface can suppress the penetrating of electromagnetic wave into the internal region of absorbent particles, due to the eddy current effect, and thereafter impairs the overall EMA efficiency. On the other hand, constructing a composite structure of micrometer scale is insufficiently assisting in excavating the potential from multicomponent compositing.

Ferromagnetic metal was also introduced into the internal surface of CNTs and some efforts were rewarded with high EMA efficiency. Chen et al.<sup>7</sup> loaded  $\gamma$ -Fe<sub>2</sub>O<sub>3</sub> inside MWNTs via a wet chemical method, in which  $\gamma$ -Fe<sub>2</sub>O<sub>3</sub> nanoparticles were randomly distributed on the internal surfaces of MWNTs. Fe nanoparticles were successfully loaded into CNTs by Che and co-workers<sup>8</sup>, but the content of Fe nanoparticles was limited to 30 wt.% or below. Some researches achieved microstructure control of the ferromagnetic nanoparticles inside the dielectric layer to satisfy the small size effect, but were unable to fabricate ferromagnetic nanofibers with high lattice integrity<sup>7,8</sup>. The scraggly distribution of ferromagnetic particles weakens factors that favor permeability, such as the high saturation magnetization and the high anisotropy, and can also block the evident cross-particle exchange coupling. Therefore, it makes sense to fabricate a nanocomposite structure by loading 1D ferromagnetic particles on the surface of the substrate dielectric shell.

In the current research,  $\alpha$ -FeOOH fibers of nanometer scale, used as precursors, were prepared by liquid-phase co-precipitation first, and the carbon shell 2–3 nanometers in the thickness was thereafter cladded on the surface of precursory  $\alpha$ -FeOOH by solvothermal method. The  $\alpha$ -FeOOH@C were subjected to hydrogen-thermal (HT) annealing to transit the FeOOH into Fe and then Fe@C composite nanotubes (Fe@C NT) were fabricated successfully. It was observed that, the carbon shell induced the forming of Fe nanotubes as a substrate via the outer-retaining constraining and that Fe@C NT retain the 1D nanostructure of the precursor completely throughout the HT annealing. The unique 1D nanocomposite structure endows Fe@C NT with high electromagnetic properties and good impedance,

which then contributes to superior EMA performance in the C-X band.

## Results and discussion

### Microstructural characterization of Fe@C nanotubes

Figure 1a provides the XRD patterns of the precursor (S-a) and Fe@C NT (S-b, S-c, S-d, and S-e) obtained from the HT annealing at different temperatures. The diffraction peaks in the XRD pattern of S-a can be indexed to the (110), (130), (020), (040), (221), (160), and (250) crystal planes of  $\alpha$ -FeOOH (JCPDS card no. 03-0249). The diffraction peaks in the XRD pattern of S-b, as shown in Fig. 1a, correspond to those of  $\alpha$ -Fe<sub>2</sub>O<sub>3</sub> (JCPDS card no. 33-0664), which suggests that the  $\alpha$ -FeOOH has dehydrated and thereafter been transited to  $\alpha$ -Fe<sub>2</sub>O<sub>3</sub> after HT annealing at 350 °C. The  $\alpha$ -FeOOH fibers can further be reduced to Fe<sub>3</sub>O<sub>4</sub> (JCPDS card no. 19-0629) when exposed to HT annealing at 450 °C, as demonstrated in the figure. Diffraction peaks of Fe<sub>3</sub>O<sub>4</sub> were rather weak, while those of FeO and Fe shaped up after the precursor was HT annealed at 550 °C. The variation in the phase composition indicated that the evolution had proceeded along the route of  $\alpha$ -FeOOH  $\rightarrow$   $\alpha$ -Fe<sub>2</sub>O<sub>3</sub>  $\rightarrow$  Fe<sub>3</sub>O<sub>4</sub>  $\rightarrow$  FeO  $\rightarrow$  Fe when the precursor was HT annealed at 550 °C, which is quite similar to the evolution observed previously in CoFe<sub>2</sub>O<sub>4</sub> particles<sup>9</sup>. Only characteristic diffraction peaks of  $\alpha$ -Fe were observed in the XRD pattern of S-e, suggesting that the precursor ( $\alpha$ -FeOOH) was completely transited to Fe after HT annealing at 650 °C for 3 h. As for S-d and S-e, the peaks of Fe coincide with the (220) and (440) crystal planes that can correspond to Fe (JCPDS card no. 06-0696). A small amount of Zn<sup>2+</sup> occupies the interstitial void of  $\alpha$ -FeOOH, which is not reflected in XRD after HT annealing. The results confirm that the Fe/C composite is successfully synthesized.

To further determine the presence of the carbon shell, we obtained the Raman spectra of FeOOH@C, as shown in Fig. 1b. The D band and G band peaks located at about 1292 and 1554 cm<sup>-1</sup>, respectively, suggested the existence of a carbon shell, indicating that the carbon shell is successfully cladded on the FeOOH fibers<sup>10</sup>. The calculated I<sub>D</sub>/I<sub>G</sub> value of 1.75 for FeOOH@C in the current research indicates the low graphitization and the presence of a high density of defects as well<sup>11,12</sup>.

The magnetic hysteresis loops of  $\alpha$ -FeOOH and Fe@C samples at room temperature are shown in Fig. 1d. It can be clearly observed that the

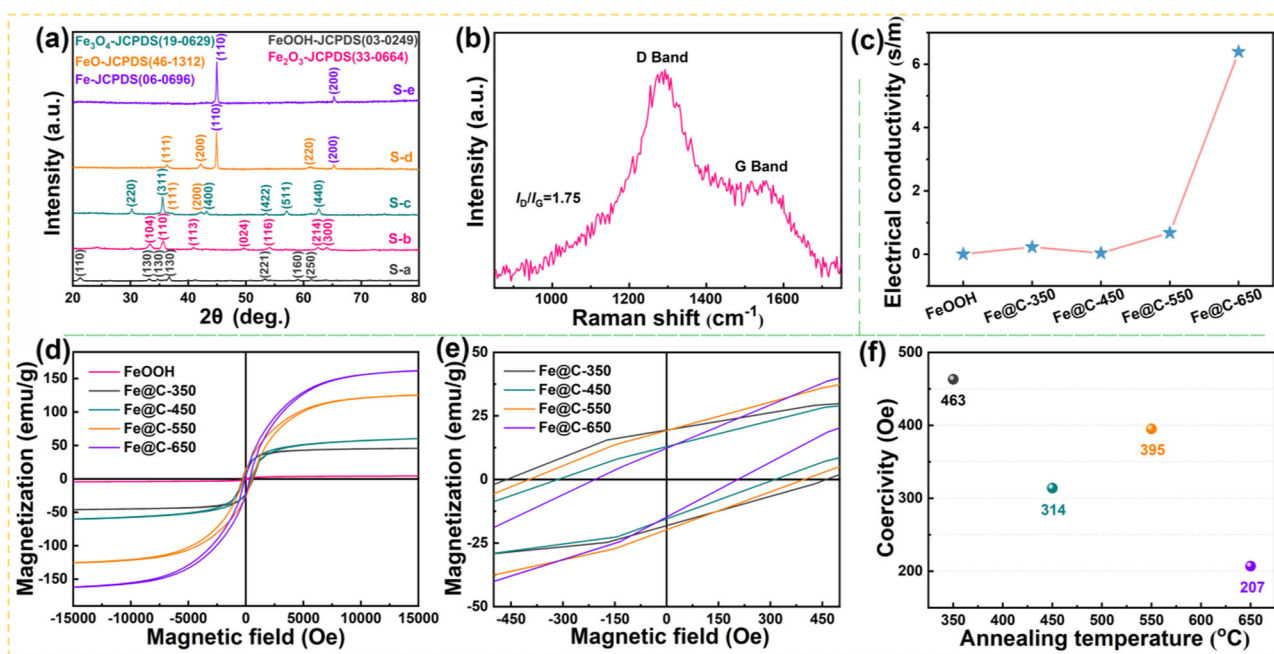


**Fig. 1 | Characterization of the Fe@C nanotubes.** a XRD patterns of  $\alpha$ -FeOOH, Fe@C-350, Fe@C-450, Fe@C-550 and Fe@C-650. b Raman spectrum of the FeOOH@C. c Average conductivity of  $\alpha$ -FeOOH, Fe@C-350, Fe@C-450, Fe@C-550,

and Fe@C-650. d, e Magnetic hysteresis loops of  $\alpha$ -FeOOH, Fe@C-350, Fe@C-450, Fe@C-550, and Fe@C-650. f Coercivity of Fe@C-350, Fe@C-450, Fe@C-550, and Fe@C-650.

precursor  $\alpha$ -FeOOH is non-ferromagnetic. The saturation magnetization ( $M_s$ ) of Fe@C-350 is much higher than that of FeOOH, which was attributed to the presence of  $\alpha$ -Fe<sub>2</sub>O<sub>3</sub> in the particles annealed at 350 °C. The  $M_s$  of Fe@C-450 is apparently higher compared to that of  $\alpha$ -FeOOH, which was due to the transition from  $\alpha$ -FeOOH to Fe<sub>3</sub>O<sub>4</sub> that occurred during the annealing. When the annealing temperature was set at 550 °C, the  $M_s$  of the product (Fe@C-550) increased substantially from 60.19 emu g<sup>-1</sup> (in the case of Fe@C-450) to 125.21 emu g<sup>-1</sup>, which is due to the generation of iron from the oxide. A high  $M_s$  of 161.64 emu g<sup>-1</sup> was observed in Fe@C-650, which is due to the complete reduction to Fe. It can be found that the  $M_s$  shows an upward trend with the increasing annealing temperature. It is obviously observed, from Fig. 1e, f, that the coercivity ( $H_c$ ) decreases gradually as the annealing temperature increases. The reduction of  $H_c$  at annealing temperature from 350 to 450 °C is due to the conversion of  $\alpha$ -Fe<sub>2</sub>O<sub>3</sub> to Fe<sub>3</sub>O<sub>4</sub>, which results in a reduced magnetocrystalline anisotropy<sup>13–15</sup>. When the annealing temperature was further increased to 550 °C, the presence of FeO, serving as domain-pinning defects in the sample, led to an increased  $H_c$ . The  $H_c$  of Fe@C-650 decreases apparently to 207 Oe. The annealing at a high temperature of 650 °C improves the lattice integrity of Fe and eliminates defects and stress, which makes the domain wall displacement and rotation easier. It is noteworthy that the  $H_c$  of all Fe@C is higher than that of the nanoparticles, which may be due to the fact that the particle size of the ferrites/ferromagnetic attached to the amorphous carbon surface is smaller than the corresponding single domain critical size, and thus the obstruction of domain wall displacement by defects and domains of surface or the increase of the pinning effect<sup>16–18</sup>.

The morphology and structure of Fe@C NT are investigated based on SEM and TEM observation, and the representative results are shown in Figs. 2, 3 and Supplementary Fig. 1. As shown in Fig. 2b, the precursor  $\alpha$ -FeOOH exhibits a well-profiled fiber morphology characterized by a diameter of about 20 nm and a length of below 1  $\mu$ m. During the preparation, ZnSO<sub>4</sub>·7H<sub>2</sub>O was used as a dopant and the doped Zn<sup>2+</sup> is a cation with a similar radius and charge as Fe<sup>3+</sup>, then it may be preferentially adsorbed in the strongest bond direction. Zn<sup>2+</sup> ions occupy the interstitial void of  $\alpha$ -FeOOH, which leads to the reduction of growth step energy and thereafter quickens the growth in the strongest bond direction and raise the aspect ratio<sup>19,20</sup>. After HT annealed at 350 °C for 3 h, the product (Fe@C-350) is identified fibers with diameter of about 30 nm and length of about 500 nm, as shown in Fig. 2c. The carbon shell, around 3 nm in thickness, can be clearly observed on the surface of Fe@C-350 (Fig. 2g). Lattice planes can hardly be distinguished in the shell, indicating that the carbon shell is of low graphitization. Intriguingly, we can distinguish the presence of voids inside the fiber in the HRTEM image of Fe@C-350. The transition from  $\alpha$ -FeOOH to  $\alpha$ -Fe<sub>2</sub>O<sub>3</sub> is a solid-state topochemical polymerization process, the escape of water vapor during the process was believed caused the cavitation process. Simultaneously, the (104) lattice plane of  $\alpha$ -Fe<sub>2</sub>O<sub>3</sub>, characterized by the interplanar spacing of 0.186 nm, can be identified, as shown in Fig. 3a, e. It can also be observed that, the voids in the fiber reduced substantially after HT annealed at 450 °C, as shown in Fig. 2d, h. Lattice planes with interplanar spacing of 0.197 nm, matching well with the (311) lattice plane of Fe<sub>3</sub>O<sub>4</sub>, are distinguished in Fe@C-450 (seen in Fig. 3b, f), confirming the analysis from the XRD result. As shown in Fig. 2e, when the annealing is performed at 550 °C, no voids can be observed, as demonstrated in the TEM images of Fe@C-550. Lattice fringes, including those of FeO (200) and Fe (110) lattice planes, are distinguished in Fig. 3c, g. The corresponding energy-dispersive spectroscopy (EDS) spectra shows that Fe@C-550 is basically composed of Fe, O, and C, and that Fe is found distributed uniformly within the C shells, as shown in Fig. 2i. It can be observed that the Fe inside the carbon shell is dense when the annealing temperature is increased to 650 °C, just as demonstrated in Fig. 2f, j. The interplanar spacing of 0.247 nm, corresponding to the (110) lattice plane of Fe, as identified from Fig. 3d, h, clearly indicates the presence of well-profiled Fe layer and the perfect crystalline lattice. These observations demonstrated that the Fe reduced from  $\alpha$ -FeOOH attached to the inner wall of the amorphous C shell and then were constructed into a sound Fe nanotube. It is quite interesting that the Fe did

not bend or agglomerate after being reduced from the  $\alpha$ -FeOOH as previously observed in varied nanocomposite particles, even though the annealing temperature of 650 °C was applied. It was believed that, the presence of amorphous carbon, serving as the outer constraining shell, can block the aggregation and thus induce the uniform paving of the Fe along the inner wall of the amorphous carbon tube.

The size of Fe@C nanotubes was quite small, specifically, the thickness of the Fe nanotubes is extremely thin. To characterize the Fe nanotube is difficult. The microstructure evolution observed in the research can demonstrate the characteristics of Fe nanotubes. The varying of cavities, voids emerge → voids disappear → the uniform paving of the Fe along the inner wall of the amorphous carbon tube, was believed to demonstrate the forming of Fe nanotubes.

This process, on the other hand, was predicted previously by referring to the two-dimensional Riemann geometry<sup>21</sup>. From the viewpoint of geometry, Riemann geometry can be divided into intrinsic one (inside the curved surface) and extrinsic one (outside the curved surface). In intrinsic geometry, both the curvature and its gradient are important factors that generate driving forces on the curvature space. Therefore, as the curved surface gets more concave, the molecules interact with more curved surfaces into the interaction range, giving rise to a stronger interaction<sup>22–24</sup>. A similar behavior was found for mercury in carbon nanotubes<sup>25</sup>. A large number of Fe nanoparticles are modified on the inner wall of the curved carbon tube to obtain a dense Fe tube. Meanwhile, atomic mobility and surface diffusion are accelerated during the HT increase, leading to uniform deposition and compact particle distribution. Thus, the tubular Fe@C nanostructure was successfully obtained. The aspect ratio of Fe@C NT obtained by HT annealing was almost unchanged compared to FeOOH@C (Supplementary Fig. 1).

### Electromagnetic parameters of Fe@C nanotubes

To investigate the microwave absorption performance and the underlying EMA mechanism of varied samples, the electromagnetic parameters are investigated and the representative results are demonstrated in Fig. 4. The complex permittivity ( $\epsilon'$  and  $\epsilon''$ ) in the range of 2–18 GHz of the specimens containing 70 wt% of  $\alpha$ -FeOOH, Fe@C-350, Fe@C-450, Fe@C-550, Fe@C-650, Fe@C-750, and Fe@C-850, respectively as fillers, are shown in Fig. 4a, b. The  $\epsilon'$  and  $\epsilon''$  of the specimen using  $\alpha$ -FeOOH as fillers fluctuate slightly within the ranges of 3.67–3.98 and 0.09–0.38, respectively, presenting weak dielectric relaxation in the band. The  $\alpha$ -FeOOH coated with C exhibit slightly increased  $\epsilon'$  after HT annealed at 350 °C, while  $\epsilon''$  remains basically unchanged compared to that in the case of  $\alpha$ -FeOOH. For specimens filled with Fe@C-450  $\epsilon'$  and  $\epsilon''$  increased from 4.02 to 13.78 and 0.32 to 2.15, respectively. When the particles annealed at 550 °C were used as fillers, the permittivity of the specimen decreased, rather than increases further, to compare with that occurred in the case of 350–450 °C.  $\epsilon'$  and  $\epsilon''$  rebound after the Fe@C nanotubes were annealed at 650 °C, compared to that in Fe@C-550, which is believed attribute to the complete conversion from  $\alpha$ -FeOOH to Fe at the high temperature. On one hand, the space-charge polarization related to Fe is further enhanced, leading to an increase of  $\epsilon'$ . On the other hand, Fe fibers can serve electric dipoles and thus promotes dipolar polarization, which can also contribute to the high permittivity. It is noteworthy that, multiple polarization peaks appear on the curve of  $\epsilon''$ , both in the case of 550 and 650 °C, suggesting that multiple polarization relaxations also cause dielectric loss besides conductivity loss<sup>18,26–28</sup>. Composite nanotubes with a high aspect ratio overlap together and construct a three-dimensional (3D) conducting network. This network disperses the electrostatic charge and thus brings about intense conductivity loss. The HT process has been carried out at 750 and 850 °C to explore the possibility of achieving higher EMA properties. It has been found that, Fe@C doesn't maintain the tubular structure but agglomerates severely after HTed at 750 or 850 °C, respectively, as shown in Supplementary Fig. 4. The electromagnetic properties have been tested to examine the effect from HT, and the results are shown in Supplementary Fig. 5.  $\alpha$ -FeOOH@C shows decreased in  $\epsilon'$  after HT annealed at 750 and 850 °C, compared to that in Fe@C-650

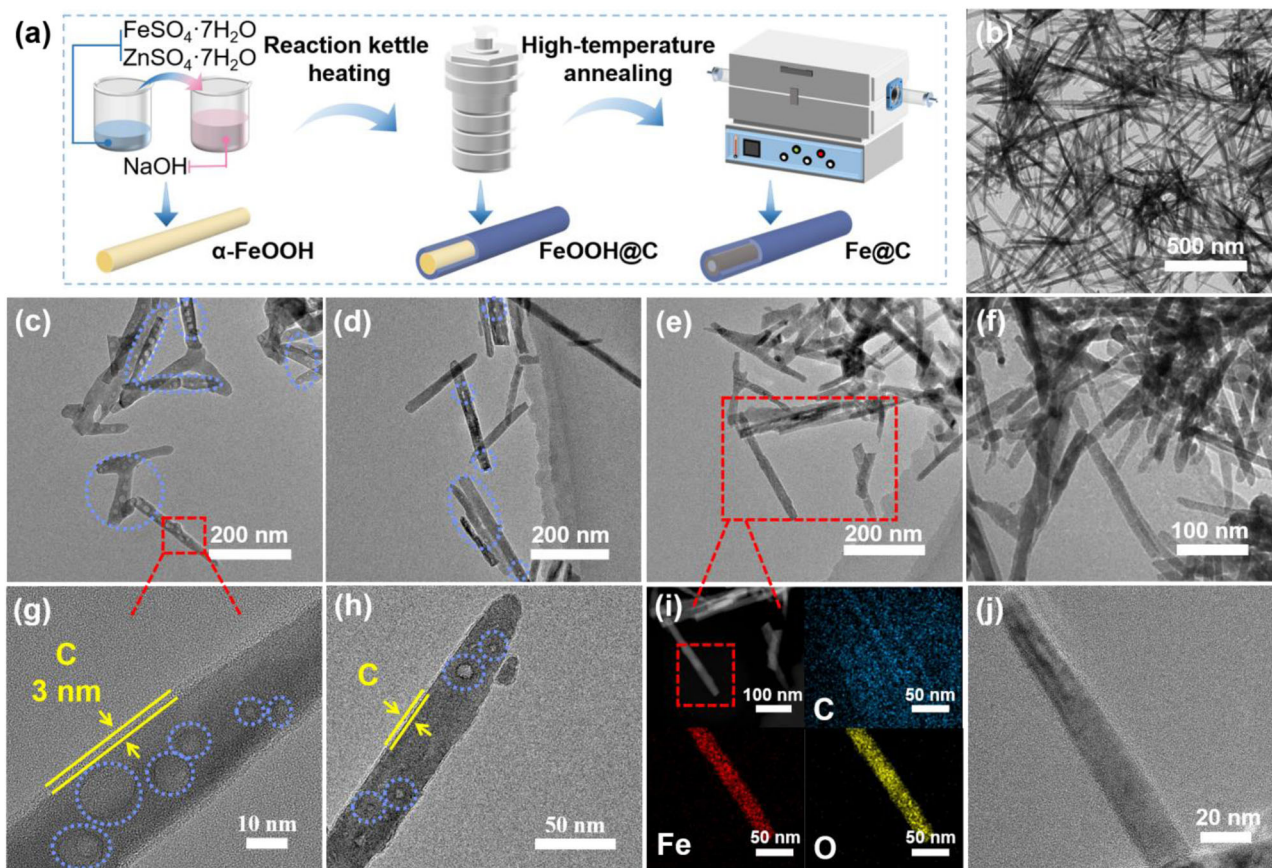


**Fig. 2 | Morphological changes in the Fe@C nanotubes during their preparation.** **a** Schematic illustration for the synthesis of Fe@C composite nanotubes. TEM images of **b**  $\alpha$ -FeOOH. **c, g** Fe@C-350. **d, h** Fe@C-450. **e** Fe@C-550. **i** the elemental mapping images of Fe@C-550. **f, j** Fe@C-650.

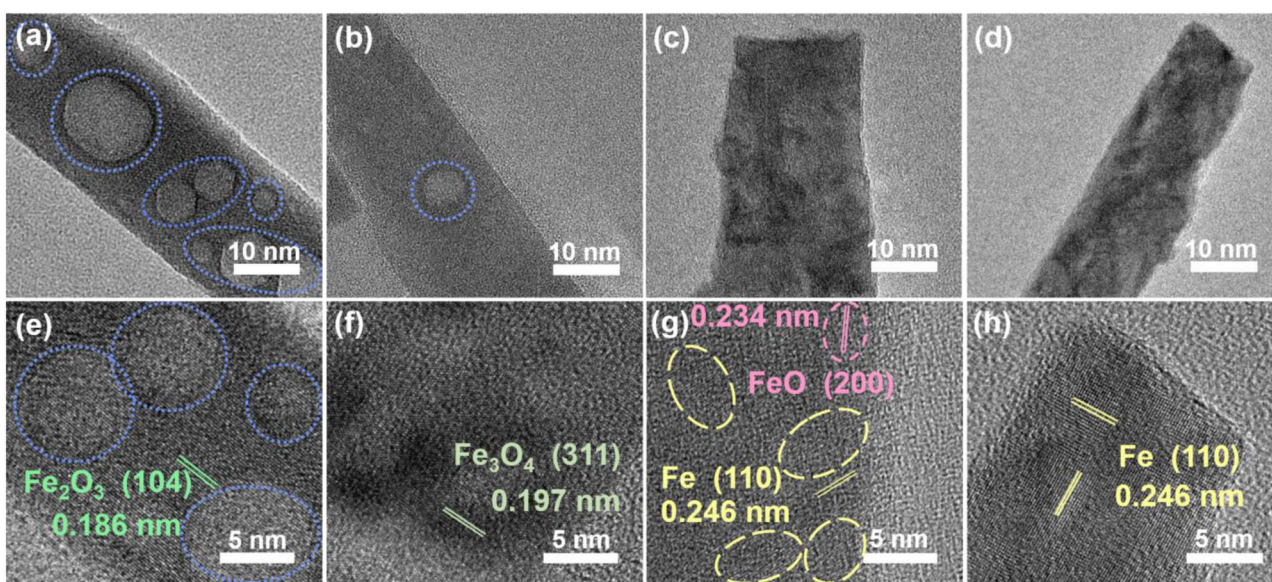


**Fig. 3 | Comparison of the morphologies of Fe@C nanotubes.** **a** TEM image of Fe@C-350 and **e** HRTEM image. **b** TEM image of Fe@C-450 and **f** HRTEM image. **c** TEM image of Fe@C-550 and **g** HRTEM image. **d** TEM image of Fe@C-650 and **h** HRTEM image.

filled specimen, which is believed attribute to the particles agglomerated severely, and the interfacial polarization and space-charge polarization are greatly reduced. Electron and ionic polarization are excluded as they are not active at frequencies below 18 GHz<sup>29,30</sup>. Hence, the dielectric loss is dominantly ascribed to conductivity loss, dipole polarization, and interfacial polarization. The enhancement of interfacial polarization can be attributed

to the unique 1D core-shell structure. Firstly, a low graphitized carbon shell will result in a surface with many defects that can become polarization centers under microwave irradiation<sup>10,31</sup>. Secondly, the interfacial polarization and the associated relaxation at the interface will occur between the core and the shell. The increase of conductivity from  $1.5 \times 10^{-3}$  to  $6.388 \text{ S m}^{-1}$ , which is attributed to the conversion from  $\alpha$ -FeOOH to Fe, contributes to

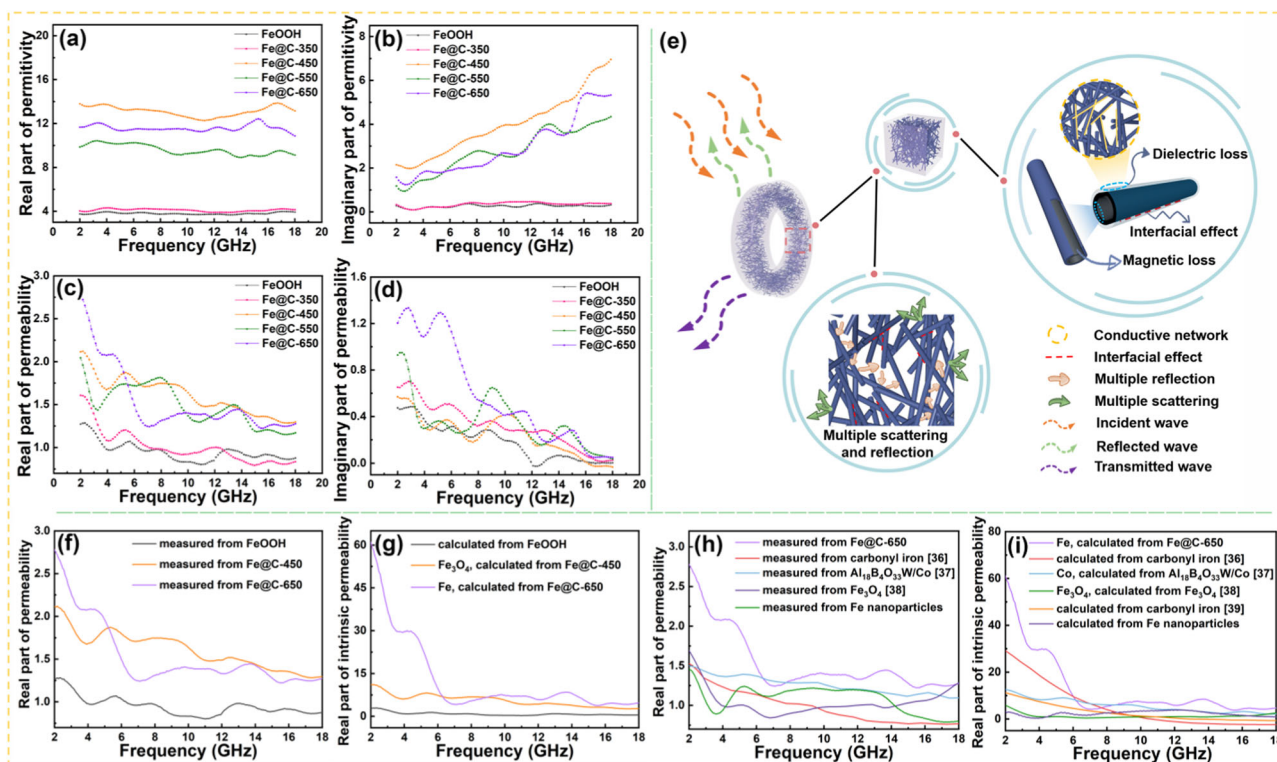


**Fig. 4 | Microwave absorbing mechanism.** Electromagnetic parameters of  $\alpha$ -FeOOH, Fe@C-350, Fe@C-450, Fe@C-550, and Fe@C-650. **a** real part ( $\epsilon'$ ), **b** imaginary part ( $\epsilon''$ ) of the complex permittivity. **c** real part ( $\mu'$ ) and **d** imaginary part ( $\mu''$ ) of the complex permeability. **e** Microwave absorption mechanism for the Fe@C composite nanotubes. **f** Measured the real part of permeability from  $\alpha$ -FeOOH, Fe@C-450, and Fe@C-650. **g** Calculated the real part of intrinsic

permeability from  $\alpha$ -FeOOH, Fe@C-450 of  $\text{Fe}_3\text{O}_4$ , and Fe@C-650 of Fe. **h** Measured the real part of permeability of Fe@C-650, carbonyl iron<sup>34</sup> and  $\text{Al}_{18}\text{B}_4\text{O}_{33}/\text{Co}$ <sup>35</sup>  $\text{Fe}_3\text{O}_4$  nanoparticles<sup>36</sup> and Fe nanoparticles. **i** Calculated the real part of intrinsic permeability of Fe@C-650 of Fe, carbonyl iron<sup>34</sup>,  $\text{Al}_{18}\text{B}_4\text{O}_{33}/\text{Co}$  of  $\text{Co}$ <sup>35</sup>  $\text{Fe}_3\text{O}_4$  nanoparticles<sup>36</sup>, carbonyl iron<sup>37</sup>, and Fe nanoparticles.

the charge accumulation and interfacial polarization at the Fe/C interface in Fig. 1c. In addition, after HT annealing, the Fe nanoparticles are densely flattened on the inner surface of the carbon shell, avoiding the agglomeration of Fe nanoparticles, and more importantly, the presence of the carbon shell maintains the morphology of the Fe nanotubes.

As observed from Supplementary Fig. 2, the dielectric loss of Fe@C-350, Fe@C-450, Fe@C-550, and Fe@C-650 is further analyzed according to the Debye relaxation theory. The polarization relaxation is generally analyzed in terms of the Cole-Cole semicircle, i.e., the semicircle presented in the  $\epsilon' - \epsilon''$  curve, representing a Debye relaxation, while the straight line segment in the  $\epsilon' - \epsilon''$  curve is related to the conductivity loss<sup>10,32</sup>. The Cole-Cole plot with Fe@C-350 as fillers is observed to have several different semicircles, indicating that Debye relaxation plays a dominant role. Based on what is known in the TEM image (Fig. 2g), there are a large number of voids in the Fe@C-350 composite fibers, which can be considered as a mixture of air and absorbent. Semicircles and line segments are observed in the Cole-Cole plots of Fe@C-450, Fe@C-550, and Fe@C-650, which indicate the simultaneous presence of Debye relaxation and conductivity loss. Fe@C-450 as fillers possesses longer line segments in the Cole-Cole plot, indicating a better conductivity loss due to the presence of soft magnetic  $\text{Fe}_3\text{O}_4$ , and dynamic electron hopping between  $\text{Fe}^{3+}$  and  $\text{Fe}^{2+}$  ions provides the intrinsic conductivity of Fe@C-450 composite fibers<sup>33</sup>. The appearance of distorted Cole-Cole semicircles in Fe@C-550 and Fe@C-650 suggests that Debye relaxation is not the sole mechanism of dielectric loss, such as Maxwell-Wagner relaxation induced by multilayer interfaces in composites.

Figure 4c, d show the complex permeability ( $\mu'$  and  $\mu''$ ) of specimens containing 70 wt% of  $\alpha$ -FeOOH, Fe@C-350, Fe@C-450, Fe@C-550, and Fe@C-650, respectively, as fillers. The  $\mu'$  of  $\alpha$ -FeOOH and Fe@C-350 filled

specimen decreases abruptly in the 2–4 GHz band and fluctuates at 0.81–1.07 and 0.79–1.21 in the 4–18 GHz band, respectively, and  $\mu''$  shows a decreasing trend with increasing frequency. Compared to  $\alpha$ -FeOOH,  $\mu'$  and  $\mu''$  of Fe@C-350 filled specimen increases from 1.25 to 1.6 and 0.45 to 0.6, respectively. The increase in permeability was related to the  $\alpha$ -FeOOH  $\rightarrow$   $\alpha$ - $\text{Fe}_2\text{O}_3$  conversion since the conversion bring about increased  $M_s$ . Although the spectra are similar, the  $\mu'$  of Fe@C-450 filler specimen are significantly higher than those in the case of Fe@C-350, which is due to the  $\alpha$ - $\text{Fe}_2\text{O}_3$   $\rightarrow$   $\text{Fe}_3\text{O}_4$  conversion from which the  $M_s$  is further enhanced. The  $\mu'$  of the Fe@C-550 filled specimen decreases surprisingly from 2.11 to 2.04 (compared with Fe@C-450) in the 2–3 GHz band, which may be due to the forming of non-ferromagnetic FeO during the annealing at the temperature of 550 °C. The  $\mu''$  of specimen filler with Fe@C-550 is much higher than that of  $\alpha$ -FeOOH, Fe@C-350 and Fe@C-450. The  $\mu'$  and  $\mu''$  of the Fe@C-650 filled specimen is found significantly higher than those of the other specimens at 2–5 GHz and 2–8 GHz bands, respectively. The increase in permeability is mainly due to the increase in Fe content. We also believe that the presence of the carbon shell contributes to the high ferromagnetic permeability, even though the carbon layer itself is essentially non-ferromagnetic. This contribution is due to the fact that the presence of the carbon shell maintains the morphology of the Fe nanotubes, and the Fe nanoparticles are reduced then in situ on the inner surface of the carbon shell, ensuring strong shape anisotropy of the ferromagnetic nanotube absorber and thus contribute to the enhanced electromagnetic properties of the nanotubes. Compared with Fe@C-650, the  $\mu'$  and  $\mu''$  are greatly reduced after HT at 750 and 850 °C, which may be attributed to the destruction of the tubular structure under high HT conditions. Further, the protective effect of the carbon shell results in significantly improved resistance to the oxidation/corrosion of the Fe core. More importantly, the cladding of the

ferromagnetic nanotubes by the carbon shell insulates the conducting in the over-lapped network, suppressing the negative effects from eddy current effects.

We have calculated the volume fraction of ferromagnetic components, based on the  $M_s$  of the components,  $\alpha$ -FeOOH,  $\text{Fe}_3\text{O}_4$ , and Fe, in the VNA specimens using  $\alpha$ -FeOOH, Fe@C-450, and Fe@C-650 as fillers, which were 20.23 vol.%, 22.77 vol.%, and 12.39 vol.%, respectively. The real part of the permeability of  $\alpha$ -FeOOH, Fe@C-450, and Fe@C-650 composites containing  $\alpha$ -FeOOH,  $\text{Fe}_3\text{O}_4$ , and Fe nanoparticles as fillers, respectively, are calculated according to the Bruggeman effective medium theory (EMT) and the medium reconstruction EMT method (MR-EMT), as shown in Fig. 4f, g. It can be observed that the calculated intrinsic permeability of  $\alpha$ -FeOOH is quite low. The Intrinsic permeability of  $\text{Fe}_3\text{O}_4$  nanoparticles, the dominating ferromagnetic component in coatings using Fe@C-450 as fillers, reaches a high level all through the 2–18 GHz band. The intrinsic  $\mu'$  of Fe nanoparticles reach the high level of 61 at 2 GHz and decreases gradually at the 2–7 GHz band and fluctuates between 3.79–8.45 at the 7–18 GHz band. The comparison shows that the intrinsic permeability of Fe nanotubes is much higher, especially at the 2–5 GHz band. Figure 4h shows the measurement results of  $\mu'$  on coatings using Fe@C-650, carbonyl iron<sup>34</sup>,  $\text{Al}_{18}\text{B}_4\text{O}_{33}\text{W/Co}^{35}$ ,  $\text{Fe}_3\text{O}_4$  nanoparticles<sup>36</sup>, and Fe nanoparticles as fillers. We can clearly observe that  $\mu'$  of coatings using Fe@C-650 as fillers is much higher than that of carbonyl iron and  $\text{Al}_{18}\text{B}_4\text{O}_{33}\text{W/Co}$  and Fe nanoparticles as fillers. Figure 4i shows the calculation of the intrinsic permeability of Fe using the MR-EMT method from the effective permeability of the samples as fillers (Fe@C-650, carbonyl iron<sup>34</sup>, carbonyl iron<sup>37</sup>, and Fe nanoparticles) with Fe content of 12.39 vol%, 20 vol%, 20 vol%, and 20.58 vol%, respectively. It can be found that the Fe nanotubes present  $\mu'$  much higher than that of carbonyl iron, Co nanoparticles, or  $\text{Fe}_3\text{O}_4$  nanoparticles.

The superior in the permeability is closely related to the unique morphology and the microstructure of the Fe nanotubes. As demonstrated in the TEM image (Fig. 2f, j), after HT annealing (650 °C), the Fe nanoparticles are continuously spread on the inwall of the carbon shell. The high saturation magnetization and high anisotropy of the Fe nanotubes contribute to the generation of high ferromagnetic resonance. On the other hand, the fine size of the Fe nanotube, together with the highly resistant amorphous carbon shell, suppresses the eddy current effect, either within individual Fe@C NT and in the whole specimen. In addition, the appearance and enhancement of cross-particle exchange coupling, due to the overlapping of 1D nanostructure, can also be contributive for achieving high permeability. Specifically, the amorphous carbon shell, 2–3 nm in thickness, insulate the Fe nanotubes from contact-conducting while conducting the cross particles coupling since the thickness is below the critical spacing<sup>38,39</sup>. The high aspect, the high lattice integrity, together with the extremely thin thickness and the insulation of the C shell, contribute together to the high intrinsic permeability, which then opens up a way for extracting the potential of ferromagnetic metallic materials in the view of permeability. The mechanism of ferromagnetic loss of the nanotubes is further determined by analyzing the variation law of the  $C_0$  ( $C_0 = \mu''(\mu')^{-2}f^1$ ) function. Since the domain wall resonance usually occurs in the low-frequency (MHz) band and the hysteresis effect at weak magnetic fields is basically negligible<sup>40</sup>. Therefore, the samples may be affected by eddy current loss, exchange resonance, and natural resonance. Supplementary Fig. 3 shows the frequency dependence of the  $C_0$  curves for all samples at 2–18 GHz. Considering that the value of  $C_0$  will be a constant if eddy current effects occur. The  $C_0$  remains essentially constant as frequency increases in the 12–18 GHz band in the case of Fe nanoparticles, indicating that eddy current loss dominates in this band. In contrast, the  $C_0$  fluctuations all through the 2–16 GHz band in the case of Fe@C-650 nanotube overlap, suggesting that the ferromagnetic loss is basically attributed to natural resonances or the exchange resonances. The presence of the C-shell maintains the shape of Fe nanotubes by avoiding the agglomeration of Fe and the fine size of Fe@C nanotubes then contribute to suppressed eddy current.

### Microwave absorbing mechanism of Fe@C nanotubes

Figure 5 and Supplementary Fig. 6 demonstrate the reflection loss (RL) of coatings, which is calculated based on the transmission line theory<sup>41,42</sup>. Supplementary Fig. 6 shows the RL of coatings using  $\alpha$ -FeOOH as fillers in the frequency range of 2–18 GHz, indicating the low EMA performance. Figure 5e–h show the effective absorption bandwidth (EAB) of these coatings. In Fig. 5a, when Fe@C-350 are used as fillers, a minimum RL ( $RL_{\min}$ ) of  $-14.16$  dB can be expected at 7.62 GHz when a thickness of 3.46 mm was applied and the EAB within which the RL is inferior to  $-10$  dB ( $WEA_{-10}$ ) reached 5.38 GHz (from 6.27 to 11.65 GHz) and RL below 5 dB ( $WEA_{-5}$ ) reached 8.71 GHz (from 3.8 to 12.51 GHz). As shown in Fig. 5b, when the thickness of the coating filled with Fe@C-450 is set at 1.7 mm, the  $RL_{\min}$  reaches  $-68.02$  dB (at 9.87 GHz) and the EAB of  $WEA_{-10}$  and  $WEA_{-5}$  are 3.85 GHz (8.23GHz–12.08 GHz) and 8.39 GHz (6.85.8GHz–15.24 GHz), respectively. The EAB of  $WEA_{-5}$  has dual-band absorption at 7.99, 9.19, and 12.65 GHz at the thickness of 3, 4, and 5 mm, respectively (Fig. 5f). At a thickness of 1.98 mm, the coating filled with Fe@C-550 shows an  $RL_{\min}$  of  $-64.34$  dB at 10.4 GHz (Fig. 5c). As can be seen from Supplementary Table 1, compared to the EMA fillers developed previously<sup>43–47</sup>, the application of Fe@C-550 present a minimum RL ( $-50.02$  dB) at 9.93 GHz amongst these materials when a small thickness of 1.33 mm is selected. Meanwhile, the EAB of 5.16 GHz is much wider than that observed previously. On the other hand, as shown in Fig. 5d, the  $RL_{\min}$  reaches  $-69.34$  dB at 3.37 GHz when the thickness of the coating filled with Fe@C-650 is set at 3.97 mm, and the EAB ( $WEA_{-10}$ ) exceeds 2.31 GHz (from 2.42 GHz to 4.73 GHz). Considering the demand from the dual-band absorbing, the series of coatings filled with Fe@C-650 is expected to present an  $WEA_{-5}$  in the 2–7.79 GHz band as well as in the 11.07–18 GHz band, covering almost the whole S-Ku band. Moreover, if the thickness was slightly increased to 5 mm, the coating using Fe@C-650 as fillers was expected to present  $WEA_{-5}$  all through the 2–18 GHz band, covering the whole S-Ku band. It can be seen that the area of high microwave absorption is mainly concentrated in the low-frequency range. The application of Fe@C ensures the coatings the high EMA efficiency and excellent compatibility, which is technically significant for developing EMA coatings.

It can be clearly observed that the attenuation constant of Fe@C-350 is synthetically higher than  $\alpha$ -FeOOH in the entire 2–18 GHz, due to the increase in ferromagnetic loss, as shown in Supplementary Fig. 7. Fe@C-450, Fe@C-550, and Fe@C-650 show relatively large attenuation constants, indicating an improvement in attenuation capability. Supplementary Fig. 8 shows the characteristic impedance of the specimens using Fe@C-350, Fe@C-450, Fe@C-550, and Fe@C-650 as fillers at varied thicknesses. The characteristic impedances of the coating using Fe@C-450 and Fe@C-550 as fillers are approximative to 1 in the high-frequency range at thicknesses of 1.7 and 1.33 mm, indicating that the coating using Fe@C-450 and Fe@C-550 as fillers have the potential to be ultrathin and perfect microwave absorbers. At a thickness of 3.97 mm, the impedance matching of the coating using Fe@C-650 as fillers is getting close to 1 in the range of 2–4 GHz, which indicates that the Fe@C-650 as fillers has good absorption performance in the low-frequency range.

In summary, the EMA mechanism of Fe@C NT can be ascribed to the following points illustrated in Fig. 4e. The presence of carbon provides favorable support for the morphological retention of Fe obtained during the annealing, which then endowed the composite particles with the superior potential of EMA capability. First, continuous Fe nanoparticles spread inside the carbon shell in the Fe@C NT structure. HT annealing reduces the spacing of Fe nanoparticles within the carbon shell, which enhances the cross-particle exchange coupling and thus improves the permeability. Second, the inter-lap of Fe nanotubes encapsulated by the carbon shell can easily build more conductive paths, which can greatly facilitate the transfer of migration and hopping electrons and play an important role in dielectric loss. Third, Fe@C NT creates abundant interfaces (e.g., Fe-C, Fe-Fe, C-C, air-C, and air-Fe interfaces) that can induce strong interfacial polarization. In addition, the presence of crystal defects in amorphous carbon shell can also lead to dipole polarization. Finally, the 1D core-shell structure includes

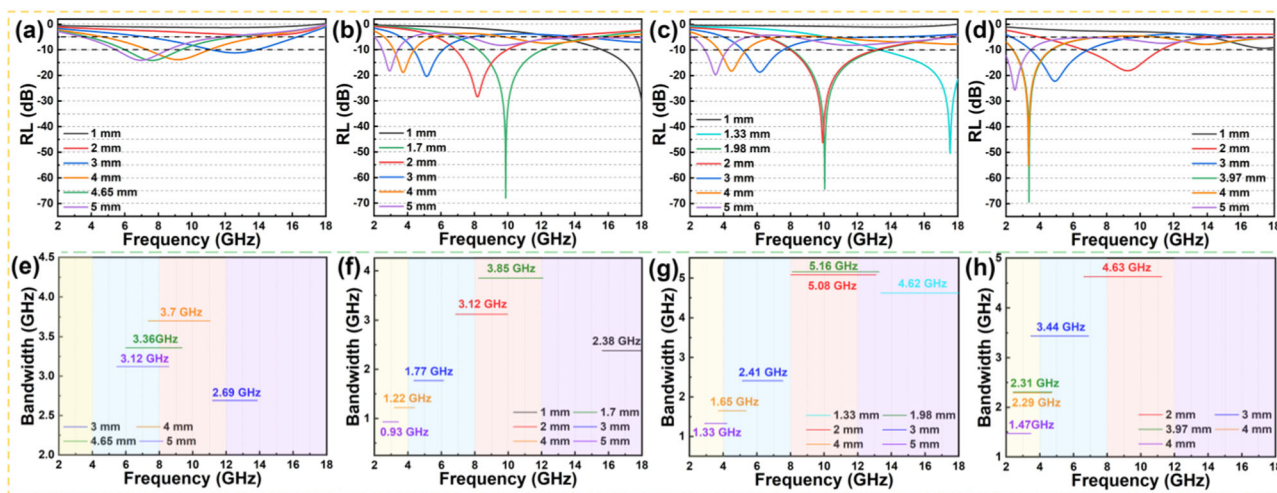


**Fig. 5 | Reflection loss versus frequency plot of absorber. a** Fe@C-350. **b** Fe@C-450. **c** Fe@C-550. **d** Fe@C-650 in the frequency range of 2–18 GHz. Reflection loss versus frequency plot and effective absorption bandwidth of **e** Fe@C-350. **f** Fe@C-450. **g** Fe@C-550. **h** Fe@C-650 in the frequency range of 2–18 GHz.

a dielectric shell (C) and magnetic core (Fe), and by adjusting the annealing temperature, the synergy of dielectric and ferromagnetic loss and better impedance matching can be achieved.

## Conclusion

In conclusion, the carbon shell was coated on the surface of precursor  $\alpha$ -FeOOH prepared via liquid-phase co-precipitation method by using a solvothermal method, followed by hydrogen-thermal annealing to obtain Fe@C composite nanotubes. Carbon shell, serving as a constraining substrate, induces the growth and maintains the shape of Fe nanotubes. The concave curvature contributes to the constraining effect of the C shell. The integrity, and the well-developed lattice of Fe nanotubes, together with the 1D nanostructure, contribute to high ferromagnetic resonance, suppressed eddy current effect, and the cross-particle exchange coupling, which then contribute to extremely high permeability. The coexistence of the Fe core and carbon shell induces a dielectric-ferromagnetic dual-loss mechanism for efficient EMW, which contributes to improved impedance matching. The unique 1D microstructure contributes to interfacial polarization and dipole polarization, which then enhances the microwave electromagnetic absorption performance. The minimum RL of coating using Fe@C-650 as fillers reaches  $-69.34$  dB at 3.37 GHz when a matching thickness of 3.97 mm was applied. The coating is predicted below  $-5$  dB in the range of 2–7.79 and 11.07–18 GHz, covering almost the whole S-Ku band. Thus, the current work paves the way for the design and preparation of 1D ferromagnetic absorbers with superior electromagnetic absorption performance.

## Methods

### Materials

Sodium hydroxide (NaOH), ferrous sulfate ( $\text{FeSO}_4 \cdot 7\text{H}_2\text{O}$ ), zinc sulfate heptahydrate ( $\text{ZnSO}_4 \cdot 7\text{H}_2\text{O}$ ), sulfuric acid ( $\text{H}_2\text{SO}_4$ ), polyvinyl pyrrolidone (PVP,  $M_w \approx 40,000$ ), glucose were purchased from Sinopharm Chemical Reagent Co. Ltd. All the chemical reagents were purchased and directly used without further purification.

### Fabrication of precursor $\alpha$ -FeOOH

Precursor  $\alpha$ -FeOOH was prepared by liquid precipitation method. Initially, NaOH (14 g) was added to deionized (DI) water (80 mL) as solution A. Afterward, the mixture of  $\text{FeSO}_4 \cdot 7\text{H}_2\text{O}$  (4 g),  $\text{ZnSO}_4 \cdot 7\text{H}_2\text{O}$  (1 g) and DI water (20 mL) acidified by sulfuric acid was stirred for 30 min to form solution B. Solution B was introduced into solution A with vigorous stirring for 30 min and then diluted with DI water (40 mL). Finally, precursor  $\alpha$ -FeOOH was formed after being stirred for 24 h. The FeOOH was finally

obtained by washing with DI water and ethanol three times and drying at  $60^\circ\text{C}$  for 12 h.

### Fabrication of precursor FeOOH@C fiber

Typically, precursor  $\alpha$ -FeOOH (0.3 g) and PVP (1.5 g) were prepared and mixed quickly under DI water (60 mL) magnetic stirring for 6 h, obtaining PVP-modified precursors  $\alpha$ -FeOOH. PVP-modified precursors  $\alpha$ -FeOOH (0.15 g) and glucose (0.18 g) were mixed in DI water (60 mL) and treated in a 100 mL Teflon lined reactor at  $180^\circ\text{C}$  for 4 h. The precursor FeOOH@C fibers were collected by washing with DI water and drying at  $60^\circ\text{C}$  overnight.

### Fabrication of Fe@C composite nanotubes

The collected precursor FeOOH@C fibers were calcined in 95% Ar and 5%  $\text{H}_2$ . The treatment temperatures were 350, 450, 550, and  $650^\circ\text{C}$  with a heating rate of  $5^\circ\text{C min}^{-1}$ , and the keeping time was 3 h. The final samples were denoted as Fe@C-350, Fe@C-450, Fe@C-550, and Fe@C-650, respectively. The schematic illustration is shown in Fig. 2a.

### Characterization

The X-ray diffraction (XRD) analysis was carried out on a PANalytical X'Pert PRO diffractometer using Cu K $\alpha$  radiation. Raman spectroscopy at green (532 nm) excitation wavelength was obtained on a Renishaw in Via-Reflex Micro. The morphology of the composite particles was observed by scanning electron microscope (SEM, FEI Quanta 200 F) and a transmission electron microscope (TEM, JEOL 2100). High-resolution transmission electron microscopy (HRTEM) observation and selected area electron diffraction (SAED) analysis were also performed on the TEM. Magnetic properties were tested on a Quantum Design MPMS3 superconducting quantum interference device (SQUID) magnetometer. The conductivity test was performed by the four-probe method, using the TEMET TM2515 DC Resistance meter. A vector network analyzer (VNA, Agilent N5230A) was used to test the electromagnetic properties of specimens in the frequency range of 2–18 GHz. The composite particles,  $\alpha$ -FeOOH, Fe@C-350, Fe@C-450, Fe@C-550, or Fe@C-650, were respectively mixed with paraffin by filling ratio of 70 wt%, homogenized thoroughly, and compressed to a coaxial toroidal to form the VNA specimens. Specimens fabricated were 6.95 mm in the outer diameter of, 3.04 mm in the inner diameter of, and around 3.0 mm in thickness.

### Data availability

The data that support the findings of this study are available from the corresponding author upon reasonable request.

Received: 26 October 2023; Accepted: 4 March 2024;

Published online: 11 March 2024

## References

- Liu, J. et al. Anion-doping-induced vacancy engineering of cobalt sulfoselenide for boosting electromagnetic wave absorption. *Adv. Funct. Mater.* **32**, 2200544–2200555 (2022).
- Guo, Y. et al. Hierarchical HCF@NC/Co derived from hollow loofah fiber anchored with metal-organic frameworks for highly efficient microwave absorption. *ACS Appl. Mater. Interfaces* **14**, 2038–2050 (2022).
- Jin, C. et al. 1D electromagnetic-gradient hierarchical carbon microtube via coaxial electrospinning design for enhanced microwave absorption. *ACS Appl. Mater. Interfaces* **13**, 15939–15949 (2021).
- Hou, Y. et al. Electrospinning of Fe/SiC hybrid fibers for highly efficient microwave absorption. *ACS Appl. Mater. Interfaces* **9**, 7265–7271 (2017).
- Wan, Y. et al. Microwave absorption properties of FeCo-coated carbon fibers with varying morphologies. *J. Magn. Magn. Mater.* **399**, 252–259 (2016).
- Zhen, L. et al. Microstructure evolution and electromagnetic properties improvement of  $\text{Al}_{18}\text{B}_4\text{O}_{33}\text{W}/\text{Co}$  composite powders through heat-treatment. *J. Magn. Magn. Mater.* **321**, 1290–1294 (2009).
- Chen, Y. et al. Gamma- $\text{Fe}_2\text{O}_3$ -mwnt/poly(*p*-phenylenebenzobisoxazole) composites with excellent microwave absorption performance and thermal stability. *Nanoscale* **6**, 6440–6447 (2014).
- Che, R. et al. Microwave absorption enhancement and complex permittivity and permeability of Fe encapsulated within carbon nanotubes. *Adv. Mater.* **16**, 401–405 (2004).
- Guan, Z. et al. Carbon-coated  $\text{CoFe}-\text{CoFe}_2\text{O}_4$  composite particles with high and dual-band electromagnetic wave absorbing properties. *Nanotechnology* **29**, 305604–305614 (2018).
- Liu, T. et al. Co/C nanoparticles with low graphitization degree: a high performance microwave-absorbing material. *J. Mater. Chem. C* **4**, 1727–1735 (2016).
- Du, Y. et al. Shell thickness-dependent microwave absorption of core-shell  $\text{Fe}_3\text{O}_4/\text{C}$  composites. *ACS Appl. Mater. Interfaces* **6**, 12997–13006 (2014).
- Ferrari, A. Interpretation of Raman spectra of disordered and amorphous carbon. *Phys. Rev. B* **61**, 14095–14108 (2000).
- Fernando, G. Magnetic anisotropy in transition metal systems. *Handbook of Metal Phys.* **4**, 110–132 (2008).
- Dunlop, D. et al. Thermoremanence, anhysteretic remanence and susceptibility of submicron magnetites: nonlinear field dependence and variation with grain size. *J. Geophys. Res.* **102**, 20199–20210 (1997).
- Besser, P. et al. Magnetocrystalline anisotropy of pure and doped hematite. *Phys. Rev.* **153**, 632–640 (1967).
- Schrefl, T. et al. Remanence and coercivity in isotropic nanocrystalline permanent magnets. *Phys. Rev. B* **49**, 6100–6114 (1994).
- Kronmuller, H. et al. Micromagnetism and microstructure of hard magnetic materials. *J. Phys. D Appl. Phys.* **29**, 2274–2283 (1996).
- Ketabi, N. et al. How functional groups change the electronic structure of graphdiyne: theory and experiment. *Carbon* **123**, 1–6 (2017).
- Wu, M. et al. Preparation and microwave characteristics of magnetic iron. *Fibers. J. Magn. Magn. Mater.* **217**, 89–92 (2000).
- Yang, M. et al. Identifying phase-dependent electrochemical stripping performance of FeOOH nanorod: evidence from kinetic simulation and analyte-material interactions. *Small* **16**, 1906830–1906840 (2020).
- Yin, Y. et al. Shape gradient and classical gradient of curvatures: driving forces on micro/nano curved surfaces. *Appl. Math. Mech.* **32**, 533–550 (2011).
- Mo, H., Evmenenko, G. & Dutta, P. Ordering of liquid squalane near a solid surface. *Chem. Phys. Lett.* **415**, 106–109 (2005).
- Chen, C. et al. Brownian motion-induced water slip inside carbon nanotubes. *Microfluid. Nanofluidics* **16**, 305–313 (2013).
- Kutana, A. Giapis Contact angles, ordering, and solidification of liquid mercury in carbon nanotube cavities. *Phys. Rev. B* **76**, 195444–195449 (2007).
- Ma, C., Chen, C., Lv, C., Xu, Z. & Zheng, Q. -S. Substrate curvature dependence of intrinsic contact angles. *Extreme Mech. Lett.* **48**, 101388–101394 (2021).
- Cheng, T. et al. Customizing the structure and chemical composition of ultralight carbon foams for superior microwave absorption performance. *Carbon* **206**, 181–191 (2023).
- Li, Z. et al. Monodispersed Co@C nanoparticles anchored on reclaimed carbon black toward high-performance electromagnetic wave absorption. *J. Mater. Sci. Technol.* **124**, 182–192 (2022).
- Zhang, M. et al. Boosted electromagnetic wave absorption performance from synergistic induced polarization of  $\text{SiCNWs}/\text{MnO}_2/\text{PPy}$  heterostructures. *Nano Res.* **16**, 3558–3569 (2023).
- Liu, J. et al. A competitive reaction strategy toward binary metal sulfides for tailoring electromagnetic wave absorption. *Adv. Funct. Mater.* **31**, 2015018–2015030 (2021).
- Guo, Y. et al. Enhancing electromagnetic wave absorption in carbon fiber using  $\text{FeS}_2$  nanoparticles. *Nano Res.* **16**, 9591–9601 (2023).
- Wu, T. et al. Facile hydrothermal synthesis of  $\text{Fe}_3\text{O}_4/\text{C}$  core-shell nanorings for efficient low-frequency microwave absorption. *ACS Appl. Mater. Interfaces* **8**, 7370–7380 (2016).
- Zhang, M. et al. An equivalent substitute strategy for constructing 3D ordered porous carbon foams and their electromagnetic attenuation mechanism. *Nano Micro Lett.* **14**, 157–178 (2022).
- Jian, X. et al. Heterostructured nanorings of  $\text{Fe}-\text{Fe}_3\text{O}_4/\text{C}$  hybrid with enhanced microwave absorption performance. *ACS Appl. Mater. Interfaces* **10**, 9369–9378 (2018).
- Wu, L. et al. Particle size influence to the microwave properties of iron based magnetic particulate composites. *J. Magn. Magn. Mater.* **285**, 233–239 (2005).
- Jiang, J. et al. Improvement on electromagnetic absorbing performance of  $\text{Al}_{18}\text{B}_4\text{O}_{33}\text{W}/\text{Co}$  composite particles through heat treatment. *Scripta Mater.* **59**, 967–970 (2008).
- Jiang, J. et al.  $\text{Fe}/\text{Fe}_3\text{O}_4/\text{mSiO}_2$  core-shell nanostructures for broadband microwave absorption. *ACS Appl. Nano Mater.* **6**, 1422–1431 (2023).
- Olmedo, L. et al. Microwave characterization and modelization of magnetic granular materials. *J. Appl. Phys.* **73**, 6992–6994 (1993).
- Kloppenburger, M. et al. Direct imaging of zero-field dipolar structures in colloidal dispersions of synthetic magnetite. *J. Am. Chem. Soc.* **126**, 16706–16707 (2004).
- Butter, K. et al. Direct observation of dipolar chains in iron ferrofluids by cryogenic electron microscopy. *Nat. Mater.* **2**, 71–72 (2003).
- Geffrin, J. M. et al. Magnetic and electric coherence in forward- and back-scattered electromagnetic waves by a single dielectric subwavelength sphere. *Nat. Commun.* **3**, 1171–1179 (2012).
- Wu, C. et al. Hollow gradient-structured iron-anchored carbon nanospheres for enhanced electromagnetic wave absorption. *Nano Micro Lett* **15**, 7–34 (2023).
- Tang, Z. et al. Synthesis of  $\text{CuCo}_2\text{S}_4$ @expanded graphite with crystal/amorphous heterointerface and defects for electromagnetic wave absorption. *Nat. Commun.* **14**, 5951–5962 (2023).
- Liu, J. R. et al. Core-shell structured Fe/ZnO composite with superior electromagnetic wave absorption performance. *Ceram. Int.* **47**, 14506–14514 (2021).
- Yi Ding, Y. et al. Electromagnetic wave absorption in reduced graphene oxide functionalized with  $\text{Fe}_3\text{O}_4/\text{Fe}$  nanorings. *Nano Res.* **9**, 2018–2025 (2016).



45. Liu, J. R. et al. Enhanced electromagnetic wave absorption properties of Fe nanowires in gigahertz range. *Appl. Phys. Lett.* **91**, 093101–093105 (2007).
46. Bao, X. et al. Excellent microwave absorption of FeCo/ZnO composites with defects in ZnO for regulating the impedance matching. *J. Alloys Compd.* **769**, 512–520 (2018).
47. Zhang, Z. et al. Porous flower-like Ni/C composites derived from MOFs toward high-performance electromagnetic wave absorption. *J. Magn. Magn. Mater.* **487**, 165334–165342 (2109).

## Acknowledgements

This work was supported by the National Natural Science Foundation of China (Grant No. 51877048, 5230010439).

## Author contributions

J.J. designed and supervised the progress of the whole project. Y.Z. proposed the idea, designed and conducted experiments, analyzed data, and drafted the article. Y.L. and C.Z. assisted with the conduction of morphology characterization and analyzed data. Z.G. Performed the VNA experiments and contributed to the discussion of the VNA results. L.Z. and J.J. supervised the research. All authors participated in the manuscript writing and approved the final version of the manuscript.

## Competing interests

The authors declare no competing interests.

## Additional information

**Supplementary information** The online version contains supplementary material available at <https://doi.org/10.1038/s43246-024-00471-x>.

**Correspondence** and requests for materials should be addressed to Zhenjie Guan or Jiantang Jiang.

**Peer review information** *Communications Materials* thanks Meng Zhang and the other, anonymous, reviewer(s) for their contribution to the peer review of this work. Primary Handling Editor: John Plummer.

**Reprints and permissions information** is available at <http://www.nature.com/reprints>

**Publisher's note** Springer Nature remains neutral with regard to jurisdictional claims in published maps and institutional affiliations.

**Open Access** This article is licensed under a Creative Commons Attribution 4.0 International License, which permits use, sharing, adaptation, distribution and reproduction in any medium or format, as long as you give appropriate credit to the original author(s) and the source, provide a link to the Creative Commons licence, and indicate if changes were made. The images or other third party material in this article are included in the article's Creative Commons licence, unless indicated otherwise in a credit line to the material. If material is not included in the article's Creative Commons licence and your intended use is not permitted by statutory regulation or exceeds the permitted use, you will need to obtain permission directly from the copyright holder. To view a copy of this licence, visit <http://creativecommons.org/licenses/by/4.0/>.

© The Author(s) 2024